Journal of
Materials Chemistry A

Materials for energy and sustainability

Accepted Manuscript

This article can be cited before page numbers have been issued, to do this please use: D. Campanella, S. Krachkovskiy, G. Bertoni, G. Gazzadi, M. Golozar, S. Kaboli, S. Savoie, G. Girard, A. C. Gheorghe, K. Okhotnikov, Z. Feng, A. Guerfi, V. Ashok, R. Gauvin, D. Bélanger and P. ANDREA, *J. Mater. Chem. A*, 2022, DOI: 10.1039/D2TA04259B.

ROYAL SOCIETY OF CHEMISTRY

rsc.li/materials-a

View Article Online
DOI: 10.1039/D2TA04259B

Metastable properties of garnet type $Li_5La_3Bi_2O_{12}$ solid electrolyte towards low temperature pressure driven densification

Daniele Campanella[1,5], Sergey Krachkovskiy[1], Giovanni Bertoni[2], Gian Carlo Gazzadi[2], Maryam Golozar[3], Shirin Kaboli[1], Sylvio Savoie[1], Gabriel Girard[1], Alina Cristina Gheorghe Nita[1], Kirill Okhotnikov[4], Zimin Feng[1], Abdelbast Guerfi[1], Ashok Vijh[1], Raynald Gauvin[3], Daniel Bélanger[5], Andrea Paolella[1,6*]

[1]Centre d'Excellence en Électrification des Transports et Stockage d'Énergie, Hydro-Québec, 1806 Boulevard Lionel-Boulet, Varennes, Québec, J3X 1S1, Canada

[2]Istituto Nanoscienze, Consiglio Nazionale delle Ricerche, Via Campi 213/A, 41125 Modena, Italy

[3]Mc Gill University, Mining & Materials Engineering Department 3610 University Street Montréal, Québec, Canada, H3A 0C5

[4]Independent researcher, 31-421 Reduta 38/9, Kraków, Poland

[5]Université du Québec à Montréal (UQAM), Département de Chimie, 2101 rue Jeanne-Mance, Montréal, Québec, H3C 3P8, Canada

[6]Austrian Institute of Technology, Battery Technologies, Giefinggasse 2, 1210, Wien, Austria

* corresponding author: andrea.paolella@ait.ac.at;

Abstract

Solid state electrolytes represent an attractive alternative to liquid electrolyte in rechargeable batteries. However, the fabrication of batteries with ceramic materials requires high temperature that could be detrimental to their electrochemical performance. In this work we show that it`s possible to densify garnet-type $Li_5La_3Bi_2O_{12}$ solid electrolyte at low temperature (600 ºC) with respect to standard high sintering temperature (T > 1000 ºC) used for zirconium-based $Li_7La_3Zr_2O_{12}$ doped garnet. $Li_5La_3Bi_2O_{12}$ showed a high conductivity (1.2×10^{-4} S cm^{-1}) after hot pressing at 600 ºC. Synthesis conditions have been optimized: at 700 ºC we observed the presence of $LiLa_2O_{3.5}$ phase as a consequence of LLBO metastability, and the formation mechanism has been described by density functional theory (DFT) and density functional perturbation theory (DFPT) calculations.

View Article Online
DOI: 10.1039/D2TA04259B

Moreover, we have reported the application of small amounts of LLBO as a sintering aid (5-10%) in the densification of LLZTO. Our investigation successfully demonstrated that LLBO introduction positively affects the densification process and global performances of LLZTO garnet, allowing to obtain an ionic conductivity higher than 10^{-4} S cm^{-1} after annealing at 600 ºC.

Introduction

In the modern days, one of the most crucial elements in taking full advantage of new renewable energy sources, is the evolution and production of reliable and efficient energy storage systems. Among the explored technologies, lithium-ion batteries[1,2] are still considered the most impactful high-performance electrochemical storage system[3]. Despite their worldwide diffusion and their noteworthy properties, a series of major challenges still require to be addressed. The use of organic flammable liquid electrolytes, in particular, represents an important safety concern that hinders the widespread deployment of this technology[4,5]. Furthermore, flammable electrolytes[6] limit the practical application of metallic lithium as anode because of the possible formation of lithium dendrites[7] that can lead to short circuits with disastrous consequences. Solid electrolytes can offer a viable alternative[8–11] to the conventional organic liquids, acting as a physical barrier against short circuits and, at the same time, increasing the energy density of the battery. In the recent years, numerous solid electrolytes based on polymeric materials[12–14], oxide or sulfide-based ceramics[15–18] and polymer-ceramic hybrid composites[19–22] were investigated and reported in literature. Li-rich garnets[15,23] such as. $Li_7La_3Zr_2O_{12}$ (LLZO) are promising candidates for practical battery applications, because of their interesting mechanical properties and high ionic conductivity, up to 10^{-4} S cm^{-1} [24]. However, full-ceramic solid electrolytes typically require strict synthesis conditions, such as high densification temperatures (well above 800 °C) over a long annealing time: LLZO with gallium[25] or aluminium[23] doping can require a synthesis temperature of 1000 °C for 10-12 h. Moreover, high synthesis temperatures are not desirable due to the evolution of side reactions with high-voltage working cathodes: for example, $LiNi_{0.6}Mn_{0.2}Co_{0.2}O_2$ (NMC622) and LLZO may lead to the formation of Li_2CO_3, $La_2Zr_2O_7$ and $La(Ni,Co)O_3$ at 700 ºC[26]. Despite these shortcomings, garnet materials exhibit the widest electrochemical stability window when compared with other classes of solid electrolytes, like NASICONs or sulfides[27]. Within

View Article Online
DOI: 10.1039/D2TA04259B

this wide family of materials, bismuth-based garnets, such as $Li_5La_3Bi_2O_{12}$ (LLBO), have been investigated due to their lower synthesis temperature (~ 800º C), as reported by Murugan et al.[23] who observed for this material a total conductivity of 1.9×10^{-5} S cm^{-1} at room temperature. A comparable value of conductivity was observed by Gao et al.[28]: a ceramic pellet compacted at 300 MPa and subsequently annealed at 750 ºC for 6 h presented a final conductivity of 2.4×10^{-5} S cm^{-1} at room temperature. Tin-replaced $Li_6La_3BiSnO_{12}$ synthesized at 785 °C displays similar values of conductivity, about 0.85×10^{-4} S cm^{-1} at room temperature[29]. Production of LLBO by quenching method[30], which involves a rapid cooling of the material to room temperature, has been shown to increase the ionic conductivity up to 2×10^{-4} S cm^{-1}[31], about ten times the value observed for the conventional synthesis. In the present work, we explored the densification mechanism of LLBO and thoroughly investigated its metastability properties, which allow a lower temperature densification, by using density functional theory (DFT) and density functional perturbation theory (DFPT) calculations. We found that hot pressing LLBO at 600º C led to a remarkable ionic conductivity (> 10^{-4} S cm^{-1}). In the present study, limited amounts of LLBO were also explored as a sintering aid for $Li_{6.4}La_3Zr_{1.4}Ta_{0.6}O_{12}$ (LLZTO) and we were able to perform the densification of Ta-doped LLZO at 600º C, achieving an ionic conductivity of 1.5×10^{-4} S cm^{-1}.

Materials and Methods

M.1 Materials and preparation. $Li_5La_3Bi_2O_{12}$ (LLBO) was synthesized via a conventional solid-state route. Anhydrous LiOH, La_2O_3 and Bi_2O_3 synthesis precursors were purchased by Sigma-Aldrich. Commercial Ta-doped LLZO (LLZTO) was purchased from Ampcera. LiOH, La_2O_3 and Bi_2O_3 were mixed in a 5.5:1.5:1 molar ratio and subsequently milled for 12 h in a Retsch PM-100 planetary ball mill. The final mixture was annealed at 775 °C in a muffle furnace for 6 h and subsequently quenched to room temperature. The LLZTO-LLBO composites were prepared by mixing LLZTO and LLBO in a SPEX mixer in the appropriate mass ratios.

M.2 Hot pressing. The resulting powders were densified by hot pressing under flowing Ar atmosphere. The pellets were prepared using about 1 g of powder. The annealing has been performed in a 16 mm Si_3N_4 die with WC mobile parts, to allow the correct

View Article Online
DOI: 10.1039/D2TA04259B

densification and avoid pellet gluing, and thin carbon paper films were set up on both sides of the powder to act as a conductive coating for the material. The final densification of LLBO was carried out at 550 °C, 600 °C, 650 °C and 700 °C for 1 h with the application of a pressure of 56 MPa, and a temperature ramp of 20 °C/min during the heating step. LLZTO/LLBO mixtures were densified at 600 °C in the same working conditions.

M.3 Scanning Electron Microscopy. Chemical mapping of the materials was performed via an energy dispersive X-ray spectrometer (EDS) in the scanning mode. Pellet cross sections were obtained using an IM4000 Plus (Hitachi, Japan) Ar ion mill with a beam sputtering energy of 6 kV, applying a fast 30° rotation for 4 h. The cross-section surfaces were investigated using a Lyra 3 (TESCAN) scanning electron microscope (SEM) and the elemental composition was obtained with an Extreme (Oxford instruments) windowless energy dispersive spectrometer (EDS). EDS maps were also acquired at higher spatial resolution from thin cross-sectional samples in a scanning transmission microscope (Thermo-Fischer Scientific Talos 200S) at an incident energy of 200 kV, along with annular dark field images (ADF) which are sensitive to the elemental composition (Z-contrast). Thin cross-sections (ca. 100 nm in thickness and with an area of few microns) were successfully obtained via focused-ion beam milling (FIB) after the deposition of a thin layer of metallorganic Pt at the surface to avoid damage and Ga implantation during milling. To enhance the signal from the EDS quantification, a compression/denoising using principal component analysis (PCA) was performed, by keeping the first 10 components in the spectral images.

M.4 Electrochemical analysis. After the densification, the resulting ceramic pellets were sandwiched between two stainless steel disks in coin cell. Electrochemical impedance spectroscopy measurements were performed with a BioLogic VMP-300 potentiostat in a temperature range from 20 to 80 °C (with a 5 °C step). The electrical conductivity of the samples was calculated considering the sample dimensions, the distance between the electrodes and the values of resistance (Ω) obtained. Cyclic voltammetry was performed in a Li//LLBO//Graphite cell at a 0.5 mV s^{-1} scan rate.

M.5 Nuclear Magnetic Resonance (NMR). ^{7}Li NMR diffusion measurement experiments were performed on 500 MHz WB Bruker AVANCE NEO NMR spectrometer using Diff50

View Article Online
DOI: 10.1039/D2TA04259B

probe and 8 mm double resonance $^{7}Li/^{19}F$ RF insert at 50 °C. A stimulated echo with longitudinal eddy current delay pulse sequence was used for the measurement. The gradient pulse was in the range of 1.0 – 1.5 ms and the diffusion time was in the range of 400 - 800 ms depending on the sample. The gradient strength was varied in 16 equidistant steps from 100 G cm^{-1} to 2500 G cm^{-1}.

M.6 Modelling. The DFT and DFPT calculations were conducted using VASP[32] in a project-augmented wave scheme. Perdew-Burke-Enzerhof exchange-correlation functional[33] was adopted. The energy cutoff was set to 500 eV and structures were relaxed until the maximum force on every atom was below 0.01 eV $Å^{-1}$. The vibrational free energies were obtained using Phonopy[34]. The representing configurations of LLBO were chosen using the program *supercell*[35] for the partial occupancy of Li in LLBO.

Results and discussions

LLBO was synthesized by solid state route (see Materials and Method section for more details) by quenching the powder at 775 ºC after 6 h of annealing, obtaining micron size particles having a pure phase as shown in **Figure 1a** while the scanning electron image (SEM) and the electron dispersion spectroscopy (EDS) mapping showing La and Bi distribution of the final product are depicted in **Figure 1b.**

View Article Online
DOI: 10.1039/D2TA04259B

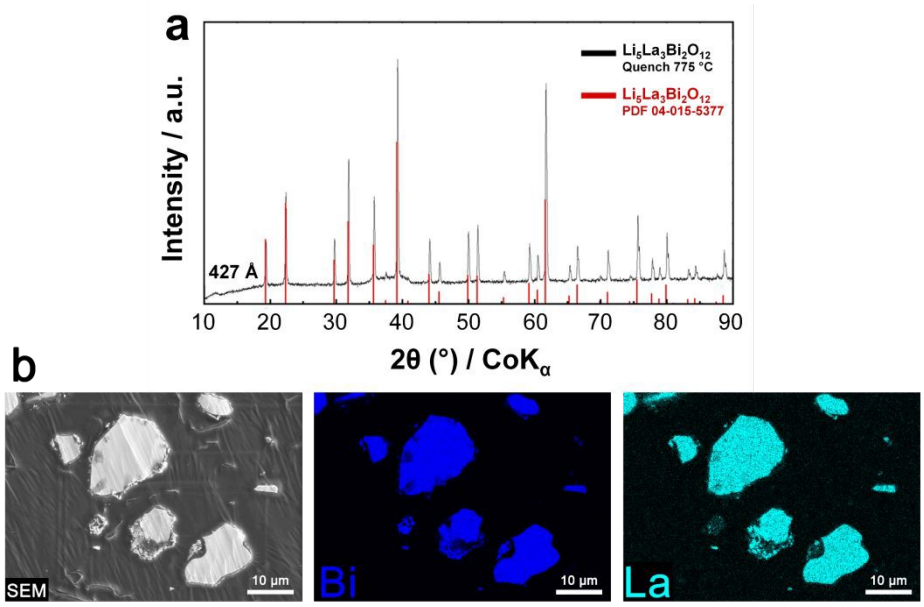

Figure 1: *a) X-rays diffraction pattern and b) EDS mapping of pristine LLBO*

To unveil the effects of different densification temperatures on the ionic conductivity of LLBO, electrochemical impedance spectroscopy measurements were performed on hot-pressed pellets in a densification temperature range from 550 to 650 °C. **Figure 2a** shows the Nyquist plots collected at room temperature for the samples annealed at 550, 600 and 650 °C and the Arrhenius plot for LLBO densified at different temperatures is reported in **Figure 2b**. **Figure 2a** also presents the equivalent circuit used for the fitting of the impedance data, in which the two separate RC elements are related to the bulk and grain boundaries contributions, respectively. The conductivity curves show a non-dissimilar impedance behavior for the materials. In particular, the samples hot-pressed at 600 ºC and 650 °C exhibit values of total ionic conductivity of about 1.2×10^{-4} S cm^{-1} at room temperature. Both values are sensibly higher than the one for the LLBO sample densified at 550 ºC, (8×10^{-5} S cm^{-1}). At higher densification temperature (700°C) the pellet is easily broken. **Figure S1** reports the values of apparent density of the LLBO samples densified at different temperatures and it shows that the density has an increasing trend with the densification temperature, reaching a value of 5.92 g cm^{-3} for the sample densified at 700 ºC, about 94% of the theoretical density value of pure LLBO (6.234 g cm^{-3})[36].

View Article Online
DOI: 10.1039/D2TA04259B

In **Figure 2c** the ADF cross-section image and the EDS elemental mappings of the LLBO sample hot-pressed at 600 °C are reported. In the image, the metallorganic Pt protecting layer deposited on the sample before FIB milling is indicated (Pt), together with the ca. 2 μm carbonate layer (*) formed at the surface. In the EDS mapping the uniform elemental distribution of La, Bi and O throughout the densified pellet can be visibly observed. The strong relative signals for O and C denote the formation of a thin carbonate layer near the surface of the sample. Moreover, the C map displays a clear presence of signals along the cracks (indicated by the arrows in the map), which point out the evolution of carbonate also at the boundaries between distinct LLBO crystals. The polycrystalline nature of lithium carbonate is confirmed by TEM observations, by which it can be observed that the respective electron diffraction pattern (reported in **Figure 2d**) shows no preferential orientation in contrast with the pattern for LLBO (**Figure 2e**).

Figure S2 shows the CV response of hot-pressed LLBO in a C//LLBO//Li cell in a potential interval between 0 and 6 V at a scan rate of 0.5 mV s^{-1}. The presence of an irreversible peak at high potential (>5 V vs Li^+/Li) can be clearly seen during the first cycle, which indicates the irreversible redox Bi^{3+}/Bi^{5+} reaction.

The cycling stability of hot-pressed LLBO towards Li is furtherly confirmed in **Figure S3**, which reports the performance of a Li//LLBO//Li symmetric cell. The measurement was carried out at a current of 0.3 mA cm^{-2} (5 h charge and 5 h discharge) and a temperature of 50 °C and, as observed from the stability curve, the cell exhibits a low polarization over a period of 300 h, indicating a high affinity of the material towards lithium.

View Article Online
DOI: 10.1039/D2TA04259B

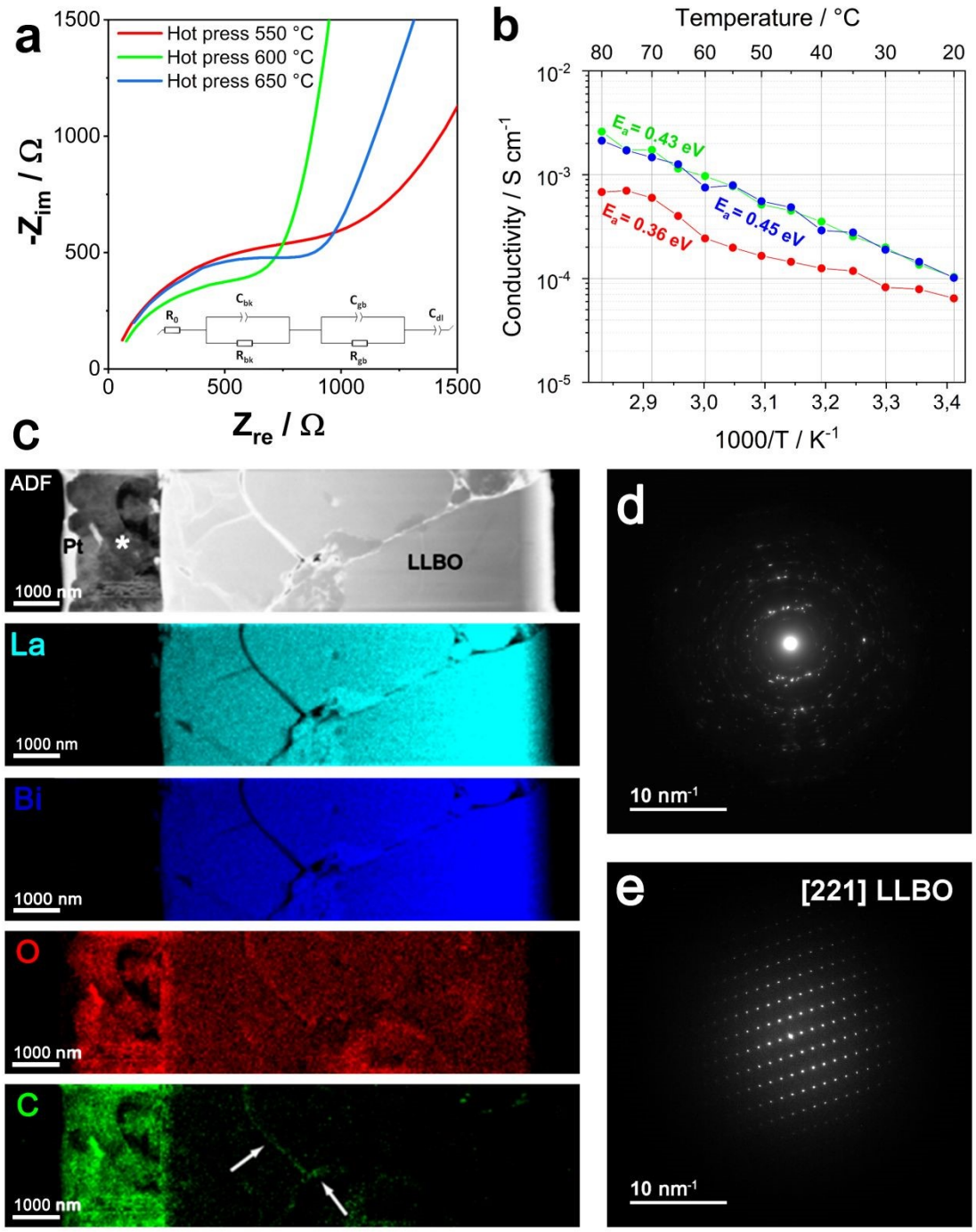

***Figure 2**: a) Nyquist plot at room temperature with equivalent circuit and b) Arrhenius plot of the hot-pressed samples at 550, 600 and 650 °C; c) STEM-obtained cross-section ADF image and EDS maps for the LLBO sample hot-pressed at 600 °C. The ADF image (top left) shows the thin cross section of the sample with the top surface of the sample on*

View Article Online
DOI: 10.1039/D2TA04259B

the left; d-e) Electron diffraction pattern of d) polycrystalline lithium carbonate and e) LLBO

Hot pressed LLBO shows a metastability range: after the hot pressing of LLBO, a sensitive increment in $LiLaO_2$ impurities can be observed while the hot pressing temperature increases, as shown in the XRD pattern in **Figure 3a**. LLBO structure undergoes an important shrinkage in the cell parameter (**Figure 3b**, red line) when passing from 650 to 700 °C, indicating the presence of a side reaction for operating temperatures higher than 650 °C. Interestingly, the crystallite size decreases when LLBO sample is annealed at 650 ºC (430 Å to 270 Å) to subsequently increase again after annealing at 700 °C (430 Å) as shown in **Figure 3b** (blue line). The cross-section SEM images and EDS mapping in **Figure 3c** shows a homogeneous distribution of La and Bi for the sample densified at 600 °C. On the other hand, the elemental distribution for the sample hot-pressed at 700 °C exhibits specific areas with a larger presence of Bi and a relatively lower presence of La, which denote a partial elemental segregation in form of Bi_2O_3 that is formed according to:

$$4Li_5La_3Bi_2O_{12} \rightarrow 4Bi_2O_3 + 6LiLa_2O_{3.5} + 7Li_2O + 4O_2\uparrow$$

Figure S4 reports a higher magnification image of LLBO hot-pressed at 600 °C, which clearly shows the uniform presence of La on the surface of the sample.

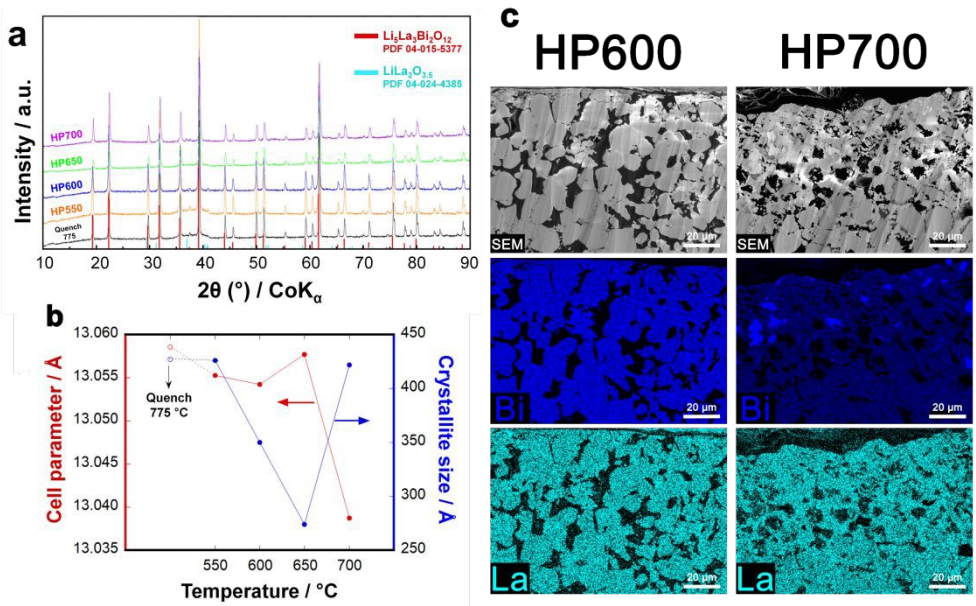

View Article Online
DOI: 10.1039/D2TA04259B

Figure 3: *a) X-rays diffraction patterns and b) evolution of cell parameter and crystallite size of the samples hot-pressed at different temperatures (550, 600, 650 and 700 °C), c) cross section SEM image and EDS elemental mapping for Bi and La of LLBO hot pressed at 600 and 700 °C*

In addition, the working equipment was not sealed, which makes the evolution of oxygen even easier. Fortunately, according to first principles calculations with harmonic approximation, the decomposition temperature of $Li_5La_3Bi_2O_{12}$ could be raised by applying external pressure. Density functional theory (DFT) and density functional perturbation theory (DFPT) calculations allowed to derive the free energies of the solid phases using harmonic approximation. Basically, the values of free energy are approximated with the sum of zero-temperature binding energy from DFT, the kinetic energies are obtained from their harmonic vibration and the temperature dependent term involving the entropy is derived from the harmonic vibration, as stated in the formula:

$$G \cong F = E_{bind} + E_{vib} - TS_{vib}$$

where the Gibbs free energy for solid phases is approximated with the Helmholtz free energy because the effect from pressure is either negligible or included in the binding energies in our case. Without anharmonicity, the partition function then becomes a well converged geometric progression, then the free energy and entropy are directly obtained from partial derivatives of it. This procedure is implemented in Phonopy[34] as a post-processing tool of the DFT calculation package VASP[32]. In addition to this, the partial occupancy of lithium ions in $Li_5La_3Bi_2O_{12}$ crystal creates further complication. In order to obtain a configuration representative enough of the actual crystal, we enumerated all possible configurations in a primitive cell of $Li_5La_3Bi_2O_{12}$ as implemented in *supercell*[35]; the configurations were sorted according to their electrostatic energies from low to high using Ewald summation, assuming point charges for the constituent ions. DFT calculations were then used to single out the configuration with minimum total energy for the subsequent free energy calculations. For the oxygen gas, the total internal energy can be split into the O_2 molecular binding energy contribution plus the kinetic energy. An offset of -1.36 eV per O_2 molecule is added to the calculated free energy at 298.15 K under 1 atm

View Article Online
DOI: 10.1039/D2TA04259B

to compensate the artificial over-binding from our computational method. Therefore, the total Gibbs energy of oxygen gas can be written as:

$$G = E + c + \frac{5}{2}RT + pV - TS = H + c - TS$$

where E is the value of binding energy from DFT, c is the constant over-binding correction, R is the gas constant, T is the temperature in Kelvin, p is the pressure (1 atm in this case, as the chamber is not sealed), V is the volume of the gas, S is the entropy and H is the enthalpy. The enthalpy and entropy of O_2 gas are adopted from JANAF tables. This way, we can estimate the Gibbs energy change for this reaction. If the change is negative, decomposition of $Li_5La_3Bi_2O_{12}$ is favored in the equilibrium state. The results of Gibbs energy change are shown in **Figure 4**. We can see that the decomposition is more and more favored as the temperature raises, in general. Without external pressure applied, the equilibrium decomposition starts above 626 K (353 °C); nevertheless, under a pressure of 0.5 kbar, the equilibrium decomposition temperature increases to 723 K (450 °C). For an ulterior increase of pressure up to 2 kbar, the decomposition temperature keeps rising up to 775 K (502 °C). Although DFT and DFPT can generate significant error in predicting temperatures, a visible tendency in the increase of decomposition temperature under applied pressure is observed. The decomposed LLBO sample after hot pressing at 700 °C is shown in **Figure 4c**.

View Article Online
DOI: 10.1039/D2TA04259B

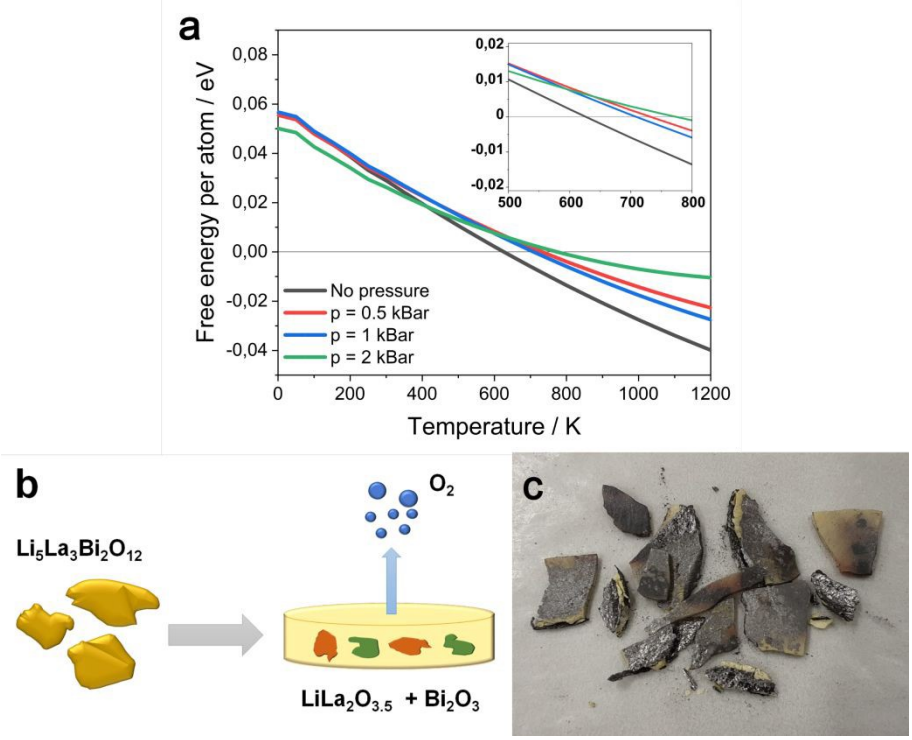

Figure 4: *a) Graph showing Free Energy vs temperature of LLBO decomposition under variation of pressure and b) Schematic of the reaction process. c) Picture of decomposed LLBO sample after thermal annealing at 700 °C.*

Considering the present results, we investigated the effects of LLBO as a sintering aid for the densification of LLZTO at 600 ºC. The Nyquist plots of pristine LLZTO and LLZTO/LLBO samples are shown in **Figure 5a**. The Arrhenius plot (**Figure 5b**) shows the conductivity trend in the range of temperature from 20 to 80 °C. The highest value of conductivity is reported for LLZTO with the addition of 10% LLBO, showing a value of 1.5×10^{-4} S cm^{-1} at room temperature, while the sample with 5% LLBO displays a slightly lower value (9×10^{-5} S cm^{-1}). Above 50 °C a trend reversal is observed and LLZTO/5%LLBO exhibits a higher conductivity than LLZTO/10%LLBO. Both samples have a superior ionic conductivity than pristine LLZTO sample (1×10^{-6} S cm^{-1}). Interestingly, the introduction of larger amounts of LLBO leads to a significant decrement in the conductivity, as observed for the sample with 30% LLBO which shows the lowest ionic conductivity at room temperature (4.9×10^{-5} S cm^{-1}). The graph reported in **Figure S5** shows the values of apparent density of a series of LLZTO/LLBO samples according to the relative LLBO content. The highest values of density are observed for the samples

View Article Online
DOI: 10.1039/D2TA04259B

prepared with 30% of LLBO, around 5.4 g cm^{-3}, whilst increasing LLBO content further leads to a decrement in density (LLZTO/50%LLBO shows a value of 4.94 g cm^{-3}. The reasons behind such a discrepancy may possibly depend on the hot-pressing process itself; high temperature treatment can lead to partial material loss which can impact the production of the pellets and the density of the material, therefor measuring effective values of density is often complicated. Additional electrochemical investigation on the material involved a cyclic voltammetry test (**Figure S6**), performed on LLZTO/10%LLBO. The pattern exhibits a broad irreversible peak at high voltages (> 4 V vs Li^+/Li) in the oxidation step during the first cycle, which may indicate the bismuth oxidation reaction from Bi^{3+} to Bi^{5+}. The cycling stability of the hot-pressed material was also investigated and **Figure S7** reports the performance of a Li//LLZO-LLBO//Li symmetric cell. Measurement was performed at a current of 0.3 mA cm^{-2} and a temperature of 50 °C. The graph reports that the symmetric cell exhibits a higher polarization compared with the cell with pristine LLBO, with an initial polarization of 1 V during both charge and discharge which slightly peters down to 0.5 V after 300 h of cycling. The presence of more resistive LLZO as a main component can explain the difference in performance between the cells, being LLZO a more resistive material than LLBO.

View Article Online
DOI: 10.1039/D2TA04259B

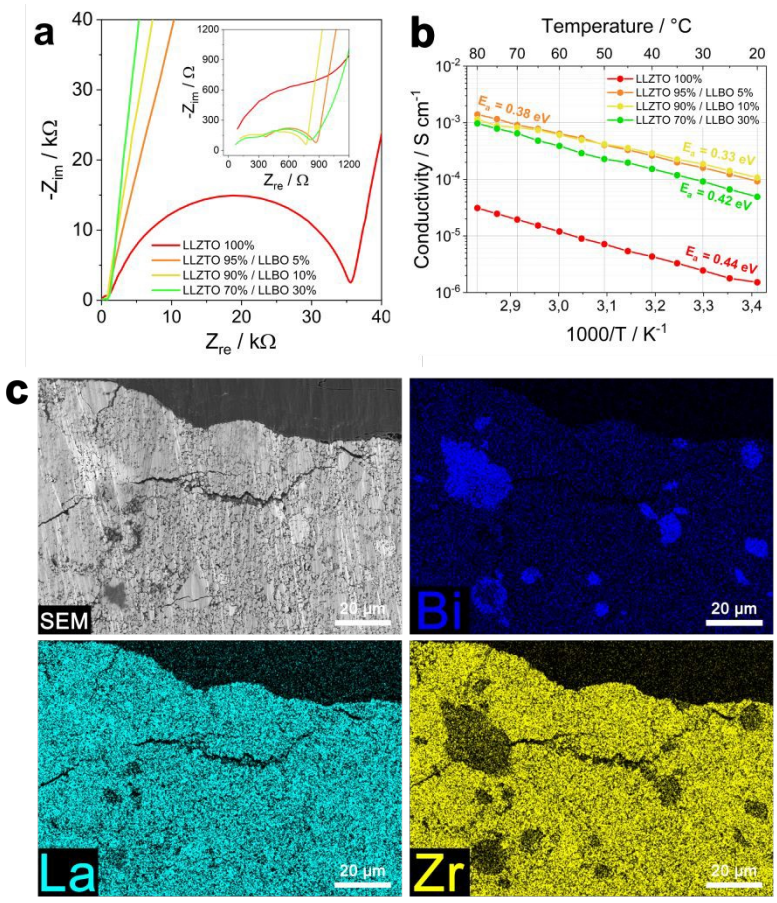

Figure 5*: a) Nyquist plots measured at room temperature and b) Arrhenius plot of the LLZTO/LLBO samples having different LLBO %; c) SEM image and EDS elemental maps for Bi, La and Zr of LLZTO/10%LLBO sample.*

The LLZTO sample containing 10% LLBO was subsequently analyzed via SEM and EDS and the presence of local LLBO-rich islands dispersed throughout the LLZTO matrix was observed, as reported in **Figure 5c.** These observations suggest the absence of a bulk reaction between the two phases of LLZTO and LLBO, while at the same time the structure of the LLBO phase is preserved. **Figure S7** shows a higher magnification SEM image of LLZTO/10%LLBO in which the uniform distribution of La on the whole surface of the pellet is clearly visible. The XRD diffraction pattern of hot-pressed LLZTO/10%LLBO is reported in **Figure S8** and it can be observed that after the hot-pressing treatment the LLZO cubic phase is preserved and no significant presence of impurities is observed in the structure.

View Article Online
DOI: 10.1039/D2TA04259B

To better understand Li transport properties of the material, Li diffusion coefficients were measured by ^{7}Li pulsed-field gradient nuclear magnetic resonance (PFG NMR) technique in LLBO samples densified at different temperatures, as well as in LLZTO with 10% of LLBO composite hot pressed at 600 °C. Short-duration magnetic field gradient pulses are introduced into spin-echo sequence to detect particles displacement in PFG NMR experiments[37]. The resulted signal intensity (I) depends on parameters of the applied gradients and the self-diffusion coefficient (D) of the observed species by the following equation: $I = I_0 e^{-BD}$, where I_0 is the NMR signal intensity without gradients application and B represents experimental conditions as: $B = \gamma^2 g^2 \delta^2 \left(\Delta - {}^{\delta}/_{3}\right)$, with γ – gyromagnetic ratio of observed nuclei, g and δ – strength and duration of the gradient pulses, Δ – delay between the encoding and the decoding gradients. An example of stacked ^{7}Li PFG NMR spectra of LLBO sample collected at different gradient strengths (g varied from 100 G cm^{-1} to 2500 G cm^{-1} in 16 equidistant steps) is shown in **Figure 6a**. The obtained values of lithium diffusion coefficients for all samples measured that way are listed in **Figure 6b**. The mean squared displacement of Li during NMR experiment could be estimated as $d = \sqrt{2Dt}$. With $D \sim 10^{-13}$ m^2 s^{-1} and with diffusion time during PFG NMR experiment $\Delta = 0.5$ s the displacement d is about 0.3 μm. This is an order of magnitude larger than the crystallite size (**Figure 3b**), but smaller than the crystal size of the analyzed compounds. It means that the obtained values of Li diffusion coefficients reflect mostly Li mobility inside secondary particles (through crystallites and grain boundaries between them), while Li transition between the particles has a negligible effect on the collected data. One can see that Li diffusion in LLBO depends on densification conditions. It means that densification at higher temperature promotes a better contact quality between crystallites decreasing the grain boundary effect. In contrast, there is no difference in Li diffusion between LLZTO and LLZTO/10% LLBO samples. Possibly, hot pressing temperature of 600 °C is not high enough to affect LLZO crystals. At the same time, a partial incorporation of LLBO, with higher Li diffusivity, increases bulk conductivity of the electrolyte (**Figure 5b**). LLBO is shown to help the densification of LLZTO by keeping secondary particles closer as reported in the scheme in **Figure 6c**.

View Article Online
DOI: 10.1039/D2TA04259B

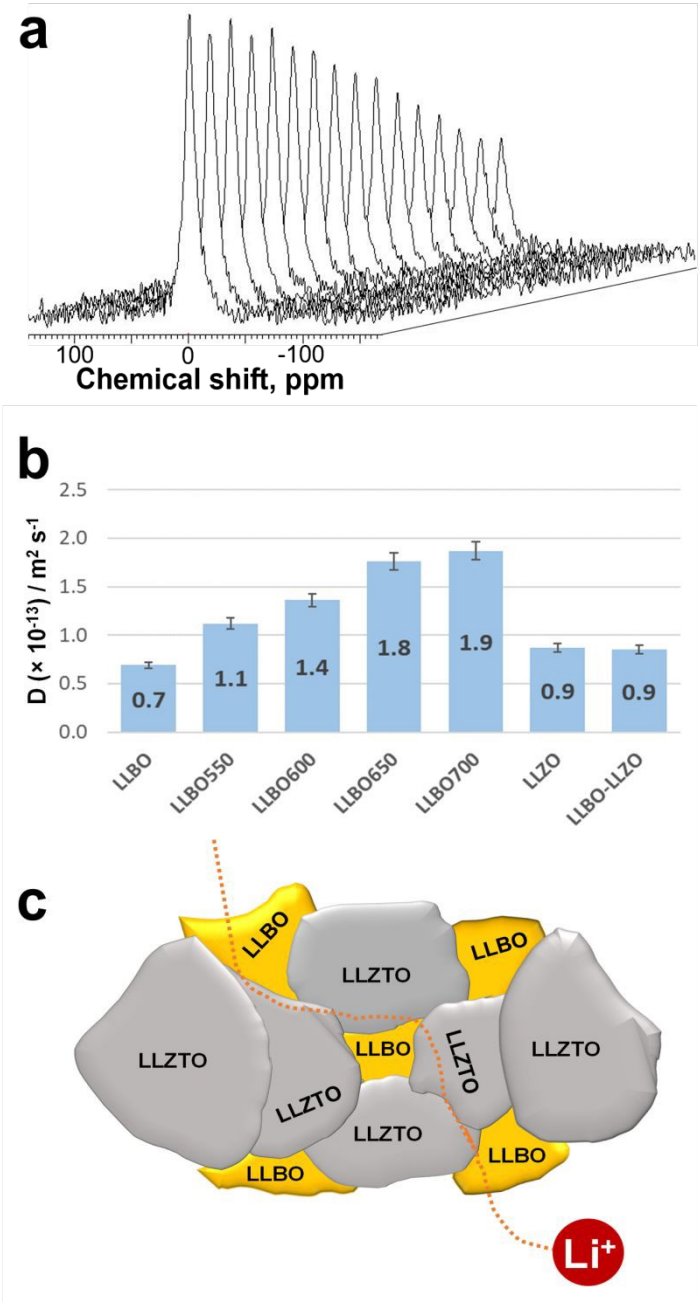

Figure 6: *a) Stacked ^{7}Li PFG NMR spectra of LLBO sample collected at different gradient strengths. b) Li diffusion coefficients measured by PFG NMR in pristine LLBO, in LLBO densified at 550, 600, 650 and 700 °C, in pristine LLZTO and in LLZTO/10% LLBO composite. c) Schematic representation of Li^{+} ion diffusion in the LLZTO/LLBO composite.*

View Article Online
DOI: 10.1039/D2TA04259B

Conclusions

In the present work we successively reported the pressure driven densification of garnet-type $Li_5La_3Bi_2O_{12}$ solid electrolyte at 600 ºC, a value of temperature significantly lower than the standard temperature (T > 1000 ºC) typically required for zirconium-based $Li_7La_3Zr_2O_{12}$. By the application of hot pressing, the densification conditions for $Li_5La_3Bi_2O_{12}$ have been optimized, leading to a high ionic conductivity of 1.2×10^{-4} S cm^{-1} after hot pressing at 600 ºC. Treatment performed at 700 ºC brought to a partial segregation of bismuth and to the formation of $LiLa_2O_{3.5}$ secondary phase as a consequence of LLBO metastability. The impurity formation mechanism has been subsequently described by density functional theory (DFT) and density functional perturbation theory (DFPT) calculations. Moreover, we demonstrated that LLBO may be usefully employed as sintering aid (5-10%) for LLZTO solid electrolyte, allowing to obtain an ionic conductivity higher than 10^{-4} S cm^{-1} after densification at low temperature (600 ºC).

Acknowledgements

This research was funded by Hydro-Québec's Center of Excellence in Transportation Electrification and Energy Storage, Varennes, Québec. A.P. want to thank dr. Chisu Kim, dr. Hendrix Demers, Daniel Clement of CEETSE (Canada) and Sergio Marras of Italian Institute of Technology (Italy) for their useful suggestions. D.C. acknowledges the financial support of Mitacs.

References

(1) Armand, M.; Tarascon, J.-M. Building Better Batteries. *Nature* **2008**, *451* (7179), 652–657. https://doi.org/10.1038/451652a.

(2) Di Lecce, D.; Verrelli, R.; Hassoun, J. Lithium-Ion Batteries for Sustainable Energy Storage: Recent Advances towards New Cell Configurations. *Green Chemistry*. Royal Society of Chemistry 2017, pp 3442–3467. https://doi.org/10.1039/c7gc01328k.

(3) Scrosati, B.; Hassoun, J.; Sun, Y.-K. Lithium-Ion Batteries. A Look into the Future. *Energy Environ. Sci.* **2011**, *4* (9), 3287. https://doi.org/10.1039/c1ee01388b.

View Article Online
DOI: 10.1039/D2TA04259B

(4) Harris, S. J.; Timmons, A.; Pitz, W. J. A Combustion Chemistry Analysis of Carbonate Solvents Used in Li-Ion Batteries. *J. Power Sources* **2009**, *193* (2), 855–858. https://doi.org/10.1016/j.jpowsour.2009.04.030.

(5) Lisbona, D.; Snee, T. A Review of Hazards Associated with Primary Lithium and Lithium-Ion Batteries. *Process Saf. Environ. Prot.* **2011**, *89* (6), 434–442. https://doi.org/10.1016/j.psep.2011.06.022.

(6) Weiss, M.; Ruess, R.; Kasnatscheew, J.; Levartovsky, Y.; Levy, N. R.; Minnmann, P.; Stolz, L.; Waldmann, T.; Wohlfahrt-Mehrens, M.; Aurbach, D.; Winter, M.; Ein-Eli, Y.; Janek, J. Fast Charging of Lithium-Ion Batteries: A Review of Materials Aspects. *Adv. Energy Mater.* **2021**, *11* (33), 2101126. https://doi.org/10.1002/aenm.202101126.

(7) Fan, L.; Wei, S.; Li, S.; Li, Q.; Lu, Y. Recent Progress of the Solid-State Electrolytes for High-Energy Metal-Based Batteries. *Adv. Energy Mater.* **2018**, *8* (11), 1702657. https://doi.org/10.1002/aenm.201702657.

(8) Li, J.; Ma, C.; Chi, M.; Liang, C.; Dudney, N. J. Solid Electrolyte: The Key for High-Voltage Lithium Batteries. *Adv. Energy Mater.* **2015**, *5* (4), 1401408. https://doi.org/10.1002/aenm.201401408.

(9) Janek, J.; Zeier, W. G. A Solid Future for Battery Development. *Nat. Energy* **2016**, *1* (9), 16141. https://doi.org/10.1038/nenergy.2016.141.

(10) Hu, Y.-S. Batteries: Getting Solid. *Nat. Energy* **2016**, *1* (4), 16042. https://doi.org/10.1038/nenergy.2016.42.

(11) Zheng, F.; Kotobuki, M.; Song, S.; Lai, M. O.; Lu, L. Review on Solid Electrolytes for All-Solid-State Lithium-Ion Batteries. *J. Power Sources* **2018**, *389*, 198–213. https://doi.org/10.1016/j.jpowsour.2018.04.022.

(12) Agrawal, R. C.; Pandey, G. P. Solid Polymer Electrolytes: Materials Designing and All-Solid-State Battery Applications: An Overview. *J. Phys. D. Appl. Phys.* **2008**, *41* (22), 223001. https://doi.org/10.1088/0022-3727/41/22/223001.

(13) Khurana, R.; Schaefer, J. L.; Archer, L. A.; Coates, G. W. Suppression of Lithium Dendrite Growth Using Cross-Linked Polyethylene/Poly(Ethylene Oxide) Electrolytes: A New Approach for Practical Lithium-Metal Polymer Batteries. *J.*

View Article Online
DOI: 10.1039/D2TA04259B

Am. Chem. Soc. **2014**, *136* (20), 7395–7402. https://doi.org/10.1021/ja502133j.

(14) Li, Z.; Li, A.; Zhang, H. H.; Lin, R.; Jin, T.; Cheng, Q.; Xiao, X.; Lee, W.-K. W. K.; Ge, M.; Zhang, H. H.; Zangiabadi, A.; Waluyo, I.; Hunt, A.; Zhai, H.; Borovilas, J. J. J.; Wang, P.; Yang, X. Q. X.-Q.; Chuan, X.; Yang, Y. Interfacial Engineering for Stabilizing Polymer Electrolytes with 4V Cathodes in Lithium Metal Batteries at Elevated Temperature. *Nano Energy* **2020**, *72* (March), 104655. https://doi.org/10.1016/j.nanoen.2020.104655.

(15) Thangadurai, V.; Narayanan, S.; Pinzaru, D. Garnet-Type Solid-State Fast Li Ion Conductors for Li Batteries: Critical Review. *Chem. Soc. Rev.* **2014**, *43* (13), 4714. https://doi.org/10.1039/c4cs00020j.

(16) Kato, Y.; Hori, S.; Saito, T.; Suzuki, K.; Hirayama, M.; Mitsui, A.; Yonemura, M.; Iba, H.; Kanno, R. High-Power All-Solid-State Batteries Using Sulfide Superionic Conductors. *Nat. Energy* **2016**, *1* (4), 16030. https://doi.org/10.1038/nenergy.2016.30.

(17) Gao, Z.; Sun, H.; Fu, L.; Ye, F.; Zhang, Y.; Luo, W.; Huang, Y. Promises, Challenges, and Recent Progress of Inorganic Solid-State Electrolytes for All-Solid-State Lithium Batteries. *Adv. Mater.* **2018**, *30* (17), 1705702. https://doi.org/10.1002/adma.201705702.

(18) Ma, Z.; Xue, H. G.; Guo, S. P. Recent Achievements on Sulfide-Type Solid Electrolytes: Crystal Structures and Electrochemical Performance. *Journal of Materials Science*. Springer New York LLC March 1, 2018, pp 3927–3938. https://doi.org/10.1007/s10853-017-1827-6.

(19) Zheng, J.; Dang, H.; Feng, X.; Chien, P.-H.; Hu, Y.-Y. Li-Ion Transport in a Representative Ceramic–Polymer–Plasticizer Composite Electrolyte: Li7La3Zr2O12–Polyethylene Oxide–Tetraethylene Glycol Dimethyl Ether. *J. Mater. Chem. A* **2017**, *5* (35), 18457–18463. https://doi.org/10.1039/C7TA05832B.

(20) Chen, L.; Li, Y.; Li, S. P.; Fan, L. Z.; Nan, C. W.; Goodenough, J. B. PEO/Garnet Composite Electrolytes for Solid-State Lithium Batteries: From "Ceramic-in-Polymer" to "Polymer-in-Ceramic." *Nano Energy* **2018**, *46* (December 2017), 176–184. https://doi.org/10.1016/j.nanoen.2017.12.037.

View Article Online
DOI: 10.1039/D2TA04259B

(21) Commarieu, B.; Paolella, A.; Daigle, J. C.; Zaghib, K. Toward High Lithium Conduction in Solid Polymer and Polymer–Ceramic Batteries. *Curr. Opin. Electrochem.* **2018**, *9*, 56–63. https://doi.org/10.1016/j.coelec.2018.03.033.

(22) Wu, N.; Chien, P.-H.; Li, Y.; Dolocan, A.; Xu, H.; Xu, B.; Grundish, N. S.; Jin, H.; Hu, Y.-Y.; Goodenough, J. B. Fast Li + Conduction Mechanism and Interfacial Chemistry of a NASICON/Polymer Composite Electrolyte. *J. Am. Chem. Soc.* **2020**, *142* (5), 2497–2505. https://doi.org/10.1021/jacs.9b12233.

(23) Murugan, R.; Thangadurai, V.; Weppner, W. Fast Lithium Ion Conduction in Garnet-Type Li7La3Zr2O12. *Angew. Chemie Int. Ed.* **2007**, *46* (41), 7778–7781. https://doi.org/10.1002/anie.200701144.

(24) Huang, Z.; Chen, L.; Huang, B.; Xu, B.; Shao, G.; Wang, H.; Li, Y.; Wang, C.-A. Enhanced Performance of Li 6.4 La 3 Zr 1.4 Ta 0.6 O 12 Solid Electrolyte by the Regulation of Grain and Grain Boundary Phases. *ACS Appl. Mater. Interfaces* **2020**, *12* (50), 56118–56125. https://doi.org/10.1021/acsami.0c18674.

(25) Rawlence, M.; Filippin, A. N.; Wäckerlin, A.; Lin, T.-Y.; Cuervo-Reyes, E.; Remhof, A.; Battaglia, C.; Rupp, J. L. M.; Buecheler, S. Effect of Gallium Substitution on Lithium-Ion Conductivity and Phase Evolution in Sputtered Li 7–3 x Ga x La 3 Zr 2 O 12 Thin Films. *ACS Appl. Mater. Interfaces* **2018**, *10* (16), 13720–13728. https://doi.org/10.1021/acsami.8b03163.

(26) Kim, Y.; Kim, D.; Bliem, R.; Vardar, G.; Waluyo, I.; Hunt, A.; Wright, J. T.; Katsoudas, J. P.; Yildiz, B. Thermally Driven Interfacial Degradation between Li7La3Zr2O12 Electrolyte and LiNi0.6Mn0.2Co0.2O2 Cathode. *Chem. Mater.* **2020**, *32* (22), 9531–9541. https://doi.org/10.1021/acs.chemmater.0c02261.

(27) Han, F.; Zhu, Y.; He, X.; Mo, Y.; Wang, C. Electrochemical Stability of Li 10 GeP 2 S 12 and Li 7 La 3 Zr 2 O 12 Solid Electrolytes. *Adv. Energy Mater.* **2016**, *6* (8), 1501590. https://doi.org/10.1002/aenm.201501590.

(28) Gao, Y. X.; Wang, X. P.; Wang, W. G.; Zhuang, Z.; Zhang, D. M.; Fang, Q. F. Synthesis, Ionic Conductivity, and Chemical Compatibility of Garnet-like Lithium Ionic Conductor Li5La3Bi2O12. *Solid State Ionics* **2010**, *181* (31–32), 1415–1419. https://doi.org/10.1016/j.ssi.2010.08.012.

(29) Peng, H.; Xiao, L.; Cao, Y.; Luan, X. Synthesis and Ionic Conductivity of

View Article Online
DOI: 10.1039/D2TA04259B

Li6La3BiSnO12 with Cubic Garnet-Type Structure via Solid-State Reaction. *J. Cent. South Univ.* **2015**, *22* (8), 2883–2886. https://doi.org/10.1007/s11771-015-2821-2.

(30) Minami, K.; Mizuno, F.; Hayashi, A.; Tatsumisago, M. Lithium Ion Conductivity of the Li2S–P2S5 Glass-Based Electrolytes Prepared by the Melt Quenching Method. *Solid State Ionics* **2007**, *178* (11–12), 837–841. https://doi.org/10.1016/j.ssi.2007.03.001.

(31) Peng, H.; Zhang, Y.; Li, L.; Feng, L. Effect of Quenching Method on Li Ion Conductivity of Li5La3Bi2O12 Solid State Electrolyte. *Solid State Ionics* **2017**, *304*, 71–74. https://doi.org/10.1016/j.ssi.2017.03.030.

(32) Kresse, G.; Furthmüller, J. Efficient Iterative Schemes for Ab Initio Total-Energy Calculations Using a Plane-Wave Basis Set. *Phys. Rev. B* **1996**, *54* (16), 11169–11186. https://doi.org/10.1103/PhysRevB.54.11169.

(33) Perdew, J. P.; Burke, K.; Ernzerhof, M. Generalized Gradient Approximation Made Simple. *Phys. Rev. Lett.* **1996**, *77* (18), 3865–3868. https://doi.org/10.1103/PhysRevLett.77.3865.

(34) Togo, A.; Tanaka, I. First Principles Phonon Calculations in Materials Science. *Scr. Mater.* **2015**, *108*, 1–5. https://doi.org/10.1016/j.scriptamat.2015.07.021.

(35) Okhotnikov, K.; Charpentier, T.; Cadars, S. Supercell Program: A Combinatorial Structure-Generation Approach for the Local-Level Modeling of Atomic Substitutions and Partial Occupancies in Crystals. *J. Cheminform.* **2016**, *8* (1), 17. https://doi.org/10.1186/s13321-016-0129-3.

(36) Peng, H.; Zhang, Y.; Li, L.; Feng, L. Effect of Quenching Method on Li Ion Conductivity of Li5La3Bi2O12 Solid State Electrolyte. *Solid State Ionics* **2017**, *304*, 71–74. https://doi.org/10.1016/j.ssi.2017.03.030.

(37) Han, K. S.; Bazak, J. D.; Chen, Y.; Graham, T. R.; Washton, N. M.; Hu, J. Z.; Murugesan, V.; Mueller, K. T. Pulsed Field Gradient Nuclear Magnetic Resonance and Diffusion Analysis in Battery Research. *Chem. Mater.* **2021**, *33* (22), 8562–8590. https://doi.org/10.1021/acs.chemmater.1c02891.